



HAL
open science

Near-IR Photoinduced Electrochemiluminescence Imaging with Structured Silicon Photoanodes

Yiran Zhao, Borja Sepulveda, Julie Descamps, Fatoumata Faye, Marcos Duque, Jaume Esteve, Lionel Santinacci, Neso Sojic, Gabriel Loget, Yoan Léger

► **To cite this version:**

Yiran Zhao, Borja Sepulveda, Julie Descamps, Fatoumata Faye, Marcos Duque, et al.. Near-IR Photoinduced Electrochemiluminescence Imaging with Structured Silicon Photoanodes. *ACS Applied Materials & Interfaces*, 2024, 16 (9), pp.11722-11729. 10.1021/acsami.3c19029 . hal-04478358

HAL Id: hal-04478358

<https://hal.science/hal-04478358v1>

Submitted on 11 Jul 2024

HAL is a multi-disciplinary open access archive for the deposit and dissemination of scientific research documents, whether they are published or not. The documents may come from teaching and research institutions in France or abroad, or from public or private research centers.

L'archive ouverte pluridisciplinaire **HAL**, est destinée au dépôt et à la diffusion de documents scientifiques de niveau recherche, publiés ou non, émanant des établissements d'enseignement et de recherche français ou étrangers, des laboratoires publics ou privés.

Near-IR Photoinduced Electrochemiluminescence

Imaging with Structured Silicon Photoanodes

Yiran Zhao,^a Borja S epulveda,^b Julie Descamps,^c Fatoumata Faye,^{d,e} Marcos Duque,^b Jaume Esteve,^b Lionel Santinacci,^f Neso Sojic,^{c} Gabriel Loget,^{a,c*} Yoan L eger^{d*}*

^a Univ Rennes, CNRS, ISCR (Institut des Sciences Chimiques de Rennes)-UMR 6226, Rennes 35000, France

^b Instituto de Microelectr onica de Barcelona (IMB-M, CSIC), Barcelona 08193, Spain

^c University of Bordeaux, Bordeaux INP, ISM, UMR CNRS 5255, Pessac 33607, France

^d INSA Rennes, CNRS, Institut FOTON-UMR6082, Univ Rennes, Rennes F-35000, France

^e present address : Alten Group, F-31300 Toulouse, France

^f Aix-Marseille Univ., CNRS, CINaM, Marseille, France

* Emails : Neso Sojic : sojic@u-bordeaux.fr , Gabriel Loget : gabriel.loget@cnsr.fr , Yoan L eger : yoan.leger@insa-rennes.fr

KEYWORDS. Photoelectrochemistry, Electrochemiluminescence, Deep reactive ion etching, IR imaging, Light-addressable electrochemistry

ABSTRACT

Infrared (IR) imaging devices that convert IR irradiation (invisible to the human eye) to a visible signal are based on solid-state components. Here, we introduce an alternative concept based on light-addressable electrochemistry (i.e., electrochemistry spatially confined under the action of a

light stimulus), that involves the use of a liquid electrolyte. In this method, the projection of a near-IR image ($\lambda_{\text{exc}} = 850$ or 840 nm) onto a photoactive Si-based photoanode, immersed into a liquid phase, triggers locally the photoinduced electrochemiluminescence (PECL) of the efficient $[\text{Ru}(\text{bpy})_3]^{2+}$ -TPrA system. This leads to the local conversion of near-IR to visible ($\lambda_{\text{PECL}} = 632$ nm) light. We demonstrate that compared to planar Si photoanodes, the use of a micropillar Si array leads to a large enhancement of local light generation and considerably improves the resolution of the PECL image by preventing photogenerated minority carriers from diffusing laterally. These results are important for the design of original light conversion devices and can lead to important applications in photothermal imaging and analytical chemistry.

1. INTRODUCTION

Light-addressable electrochemistry allows for spatial confinement of redox reactions at locally-illuminated semiconductor electrodes.^{1,2} In this concept, a focused incident light, whose energy is larger than the semiconductor bandgap, is projected on a depleted surface (i.e., a photoelectrode), immersed in a liquid electrolyte. In these conditions, the redox reaction is expected to occur only at the illuminated site and to be inhibited in the dark region.¹⁻⁵ However, in many cases, photogenerated minority charge carriers may be found several micrometers away from the illuminated site because of their lateral diffusion.⁶ As a result, the electrochemically active area can be much larger than the illuminated one. Light-addressable electrodeposition has been early employed to reveal static light patterns projected onto a semiconductor.⁷ In a recent work, amorphous Si (a-Si) has been proven an efficient material for light-addressable electrochemistry,⁸ because of its reduced carrier diffusion length (L_D) compared to crystalline Si. In this frame, a-Si has been employed as a substrate for the light-addressable electrodeposition of Pt,⁹ NiMo⁹, and Cu₂O nanoparticles¹⁰ and, more recently, for the light-addressable release of single cells.¹¹

Electrochemiluminescence (ECL) is the generation of light induced by an electrochemical reaction. It generally produces the excited state of a luminophore at an electrode surface, leading to the emission of visible photons.^{12,13} It has been widely used in clinical assays, sensing, imaging, and microscopy, especially with the following water-based anodic co-reactant ECL systems: *i*) tris(bipyridine)ruthenium(II) complex with tripropylamine ($[\text{Ru}(\text{bpy})_3]^{2+}$ -TPrA) and *ii*) 3-aminophthalhydrazide with hydrogen peroxide (luminol-H₂O₂).¹⁴⁻¹⁷ Photoinduced electrochemiluminescence (PECL) is an ECL variant that is based on photogenerated charge transfer at the semiconductor/liquid interface.¹⁸⁻²⁴ Because it converts optical signals through a photoelectrochemical mechanism, PECL can, in principle, also be employed for revealing

projected patterns, which is particularly interesting when the excitation wavelength is invisible to the human eye. Localized PECL photoconversion of visible light ($\lambda_{\text{exc}} = 674$ to $\lambda_{\text{ECL}} = 413$ nm) via the annihilation of a diphenylanthracene derivative on *p*-Si has been early mentioned by Bard *et al.*¹⁹ and, more recently, Ciampi *et al.* have reported local visible light ($\lambda_{\text{exc}} = 625$ to $\lambda_{\text{ECL}} = 430$ nm) photoconversion with the luminol-H₂O₂ co-reactant ECL system on *n*-Si protected with a covalently grafted monolayer.²⁵ PECL has also been reported for imaging single cells and the photoelectrochemical activity of single gold nanoparticles.^{21,26} IR-to-visible light conversion was proposed in the 70's,²⁷ however, this was not practically achieved until 2020 with the model [Ru(bpy)₃]²⁺-TPrA ECL system on a Si-based metal-insulator-semiconductor (MIS) photoanode ($\lambda_{\text{exc}} = 840$ to $\lambda_{\text{ECL}} = 632$ nm).²⁸ In the two cited examples,^{25,28} photogenerated holes simultaneously oxidize the luminophore and the co-reactant in the liquid phase and the oxidized species react together to generate the excited state of the luminophore, leading to visible light emission. In the present article, localized IR-to-visible PECL conversion is studied at MIS *n*-Si/SiO_x/Ir photoanodes with the [Ru(bpy)₃]²⁺-TPrA ECL system (**Figure 1a**). It is shown that replacing planar Si by a surface structured with micropillars (Si_{IMPs}, **Figure 1b**) allows for significant improvement of the spatial resolution and light sensitivity. Finally, such photoanodes are employed for near-IR imaging.

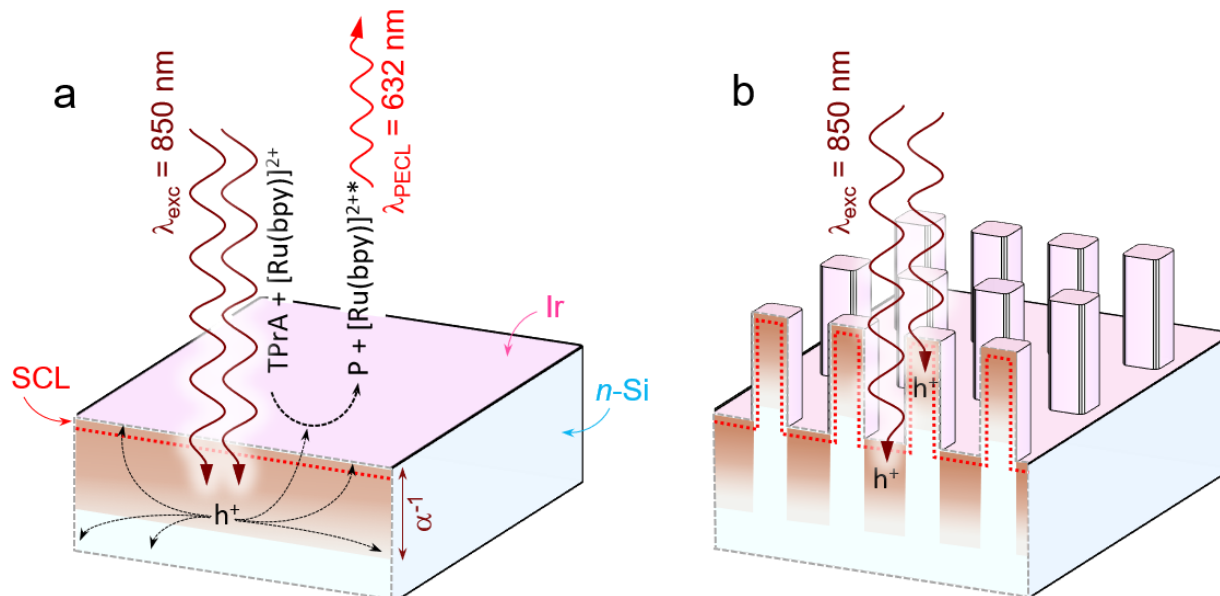


Figure 1. a) Sketches showing the generation and diffusion of holes within (a) $n\text{-Si}_{\text{plan}}/\text{SiO}_x/\text{Ir}$ and (b) $n\text{-Si}_{\text{IMPs}}/\text{SiO}_x/\text{Ir}$ photoanodes during PECL emission of $[\text{Ru}(\text{bpy})_3]^{2+}$ -TPrA. α^{-1} is the light penetration depth (gradient of brown color) and P represents the degradation products of TPrA. The space charge layer (SCL) is depicted by a red dotted line.

2. EXPERIMENTAL METHODS AND MATERIALS

2.1 Materials and reagents

The n -type silicon wafers (1-10 Ω cm resistivity, phosphorus-doped, single side polished, 475-525 μm) (100) were purchased from University Wafers. The ultrapure water had a resistivity of 18.2 $\text{M}\Omega$ cm (Purelab Classic UV). Tris(bipyridine)ruthenium(II) chloride ($\text{Ru}(\text{bpy})_3\text{Cl}_2$), tri- n -tripropylamine (TPrA) were purchased from Sigma Aldrich. Phosphate buffer solution (PBS, 100 mM, pH 7.4) was prepared from sodium phosphate dibasic heptahydrate and sodium phosphate monobasic monohydrate that were purchased from Sigma Aldrich.

2.2 Preparation of the surfaces

Si_{MP} arrays were fabricated on a $15 \times 15 \text{ mm}^2$ n -Si wafer ($\rho = 1\text{-}10 \ \Omega \text{ cm}$). For that, first, a 400-nm-thick SiO_2 layer was grown through thermal oxidation. Next, a photolithography process was carried out using direct laser writer (DLW). In this photolithography process, a layer of $1.2 \ \mu\text{m}$ resist was first deposited by spin coating. Then, the resist was exposed to light with the DWL (Disale 650) and developed. The designed pattern exposed with the DWL consists of $10 \times 10 \ \mu\text{m}^2$ squares separated by $10 \ \mu\text{m}$ from each other in a $3 \times 3 \text{ mm}^2$ square at the right center of the wafer. Subsequently, the exposed SiO_2 layer was removed by reactive ion etching (RIE) Alcatel AMS-110-DE (gasses $\text{CH}_4/\text{C}_4\text{F}_8/\text{He}$, flows 30/20/20 sccm, pressure 7 mTorr, power 2500W) using the resist mask. Next, the $20 \ \mu\text{m}$ deep Si etching was carried out by RIE Bosch process (gases $\text{CH}_4/\text{C}_4\text{F}_8$, flows 300/150 sccm, ICP power 2000W, chuck power 15W). Finally, the initially grown SiO_2 layer on top of the pillars was removed by RIE. The 2 nm-thick Ir thin films were deposited on the cleaned and oxidized $n\text{-Si}_{\text{plan}}\text{-Si}_{\text{MPs}}/\text{SiO}_x$ surfaces by sputtering with a Leica EM ACE600 coating system (Ir target purity: 99.95%). The angle between the Ir target and the substrate is 70° . The Ar pressure for sputtering was 2×10^{-2} mbar and the current 100 mA (pre-sputtering time of 1 min). After deposition, the system was degassed with N_2 .

2.3 Characterization of the photoanodes

Scanning electron microscopy (SEM) was performed using a JSM 7100F (JEOL) on an unmodified $n\text{-Si}_{\text{MPs}}/\text{SiO}_x$ electrode (Figure S1). 45° tilted SEM with compositional mode was performed using ThermoScientific APREO 2C high-vac on $n\text{-Si}_{\text{MPs}}/\text{SiO}_x/\text{Ir}$, as shown in Figure 2b,c, and Figure S2. XPS data was been collected on $n\text{-Si}_{\text{MPs}}/\text{SiO}_x/\text{Ir}$ by a Thermo-Fisher NEXSA G2 spectrometer using the Al $K\alpha$ X-ray source working at 1486.6 eV and using a spot size of $200 \ \mu\text{m}$. Binding energies were referenced to C1s peak at 285 eV.

2.4 Electrode fabrication

The $n\text{-Si}_{\text{plan}}\text{-Si}_{\text{MPs}}/\text{SiO}_x/\text{Ir}$ surfaces were processed to fabricate the electrodes. An Ohmic contact was done on the backside of Si wafer by scratching the surface with a diamond glass cutter; then a droplet of InGa eutectic (Sigma Aldrich, 99.99%, metals basis) and a copper tape was applied on the scratched part. A thin layer of silver paste (Electron Microscopy Sciences) was painted to cover the InGa eutectic contact as well as a part of the copper tape. After the drying of the paste, Kapton tape was deposited to shield the backside for the protection of Ohmic contact.

2.5 Conventional photoelectrochemical measurements

The conventional photoelectrochemical measurements (Figure 2e-f) were performed with a Biologic SP-300 potentiostat, with $n\text{-Si}_{\text{plan}}\text{-Si}_{\text{MPs}}/\text{SiO}_x/\text{Ir}$ as the working electrode, Ag/AgCl (3 M KCl) as the reference electrode and a carbon rod as the counter electrode. The electrolyte was composed of 5 mM $[\text{Ru}(\text{bpy})_3]^{2+}$, 100 mM TPrA in PBS solution (pH adjusted to 7.4). The immersed working electrode surface was 0.5 cm^2 , containing a square of $3\times 3\text{ mm}^2$ $\text{Si}_{\text{MPs}}/\text{SiO}_x/\text{Ir}$ region on the right, the rest being $\text{Si}_{\text{plan}}/\text{SiO}_x/\text{Ir}$, as shown in the inset of Figure 2f. Cyclic voltammograms (CVs) were recorded on the $n\text{-Si}_{\text{plan}}\text{-Si}_{\text{MPs}}/\text{SiO}_x/\text{Ir}$ electrode under full surface illumination with a near-IR LED (Thorlabs M850L3, $\lambda_{\text{exc}} = 850\text{ nm}$, $P_{\text{LED}} = 5\text{ mW cm}^{-2}$) or in the dark, using the optical setup previously described.²⁸ Chronoamperograms (CAs) were recorded with full surface illumination using a near-IR LED ($\lambda_{\text{exc}} = 850\text{ nm}$, $P_{\text{LED}} = 5\text{ mW cm}^{-2}$) at $E = 0.9\text{ V vs Ag/AgCl}$ with an electrolyte flow of 1 mL s^{-1} .

2.6 Light-addressable PECL and Near-IR imaging measurements

Localized PECL measurements (Figure 3) were performed with a 3-electrode setup, connected to a potentiostat PGZ100 VoltaLab from Radiometer Analytical with the optical setup shown in

Figure 3a. A table-top microscope setup featuring a x10 0.25NA long-working distance Mitutoyo objective, an 805nm shortpass dichroic filter (Thorlabs DMSP805R), a 10cm tube lens, an additional 750nm shortpass filter (Thorlabs FESH0750), a X10 microscope eyepiece and an OPPO A9 cellphone camera (fixed gain, controlled time exposure, fixed ∞ -focus, 8bit pixel depth on each color channel) was used to focus laser beams and IR images on the electrode and record the PECL signal (see Figure S5). This setup has a spatial resolution of 5 μ m when operating on an immersed electrode. The near-IR laser beam ($\lambda_{\text{exc}} = 840 \text{ nm}$) was first focused on a reference lithography mask to measure the laser spot width to be 60 μ m at the location of the photoelectrochemical cell (Figure S4). $E = 0.85 \text{ V vs Ag/AgCl}$ was applied to the $n\text{-Si}_{\text{plan}}\text{-Si}_{\text{MPs}}/\text{SiO}_x/\text{Ir}$ photoanode in the same electrolyte, as described in Section 1.5, first, on the planar Si region (Figure 3b) and, then, on the SiMPs region (Figure 3d). Figure S6 provides the raw data images of these measurements in pixel count. The near-IR imaging measurements (Figure 5) were performed with a 3-electrode setup, connected to the PGZ100 potentiostat in the optical setup shown in Figure 5a and Figure S5. The near-IR light pattern (Figure 5 b,d) was projected from a liquid-crystal-on-silicon spatial light modulator (LCOS-SLM) from HOLOeye to the electrode biased to $E = 0.85 \text{ V vs Ag/AgCl}$. In this setup, the incident LED light was reflected by a non-polarizing beam-splitter (BS) onto a polarizer with a polarization axis at 45° compared to the fast and slow axes of the SLM. Grey values of the images sent to the SLM correspond to specific dephasing between the fast and slow axis field contributions reflected by the device. They control the polarization state of the light field after reflection. The two grey values corresponding to *i*) no polarization rotation at the SLM reflection and *ii*) a 90° rotation of the field at the reflection, were used to project patterns on the electrode, providing the optimal contrast of the illumination patterns

at the working wavelength (**Figure 5b**). PECL pictures were analyzed with ImageJ and Igor Pro softwares.

3. RESULTS AND DISCUSSIONS

As depicted in **Figure 1a**, photogenerated holes are produced inside the semiconductor, within the light penetration depth (α^{-1}). In the case of crystalline Si, with the illumination wavelength used in our experiments ($\lambda_{\text{exc}} = 850 \text{ nm}$) holes are thus mainly generated within a depth of around $15 \mu\text{m}$.²⁹ The minor fraction of holes generated within the space charge layer (SCL), exhibiting a much narrower width ($0.1 > W_{\text{sc}} > 1 \mu\text{m}$), is directly driven to the solid/liquid interface, while the major part of photocarriers is generated more deeply and diffuses freely before reaching the SCL and being injected into the electrolyte. Due to the large hole diffusion length ($L_D \approx 300 \mu\text{m}$) in Si photoelectrodes, lateral diffusion in the millimeter range was reported.²⁸ It is therefore difficult to achieve localized PECL processes on planar semiconductors and it strongly limits the potential use of Si for such imaging applications. To overcome this obstacle and laterally confine photogenerated carriers at the illumination location, we propose to employ structured Si surfaces, as shown in **Figure 1b**. In this case, the region where holes are photogenerated is not continuous and their free diffusion should significantly be shortened.

3.1 Preparation and characterization of the surfaces

Silicon micropillar (Si_{MP}) arrays were fabricated on photoactive planar *n*-type Si ($n\text{-Si}_{\text{plan}}$) wafers by photolithography and deep reactive ion etching (RIE) (details are provided in Section 1.2, SI). The scanning electron microscopy (SEM) top and side view images of **Figure 2a,b** show that the Si_{MPs} have a $10 \times 10 \mu\text{m}^2$ square section, a height of $20 \mu\text{m}$, and are arrayed with a pitch of $20 \mu\text{m}$

(**Figure S1**). In addition, the pillars' side walls exhibit a periodic substructure (ripples) in the μm -length scale, which is a typical feature of the deep RIE Bosch process.³⁰ To promote charge transfer at the solid/liquid interface and avoid electrical passivation that generally occurs on bare Si anodes and leads to their rapid deactivation,^{31–34} an Ir thin film (nominal thickness = 2 nm) was deposited onto the Si_{MP} array by magnetron sputtering (details are provided in Section 1.2, SI). This was performed to create a $n\text{-Si/SiO}_x/\text{Ir}$ MIS junction, which has been proven particularly efficient for promoting photogenerated charge transfer at Si photoanodes over a long time, in the field of water splitting^{35–40} and PECL.^{28,41,42} Backscattered SEM images (**Figure S2**) of single pillars revealed that the sputtering process produced a conformal Ir thin film on the top of the pillars and a gradient of isolated Ir nanoparticles (NPs) on the pillars' sidewalls (**Figure 2c**), as well as on the inner space (Figure S2d). X-ray photoelectron spectroscopy (XPS, **Figure 2d**) confirmed the SEM observation, by exhibiting intense Ir 4f, 4d, and O 1s peaks (attributed to Si and Ir surface oxides), less intense Si 2p, 2s peaks and weak C 1s and N 1s peaks (attributed to adventitious contaminants).⁴³

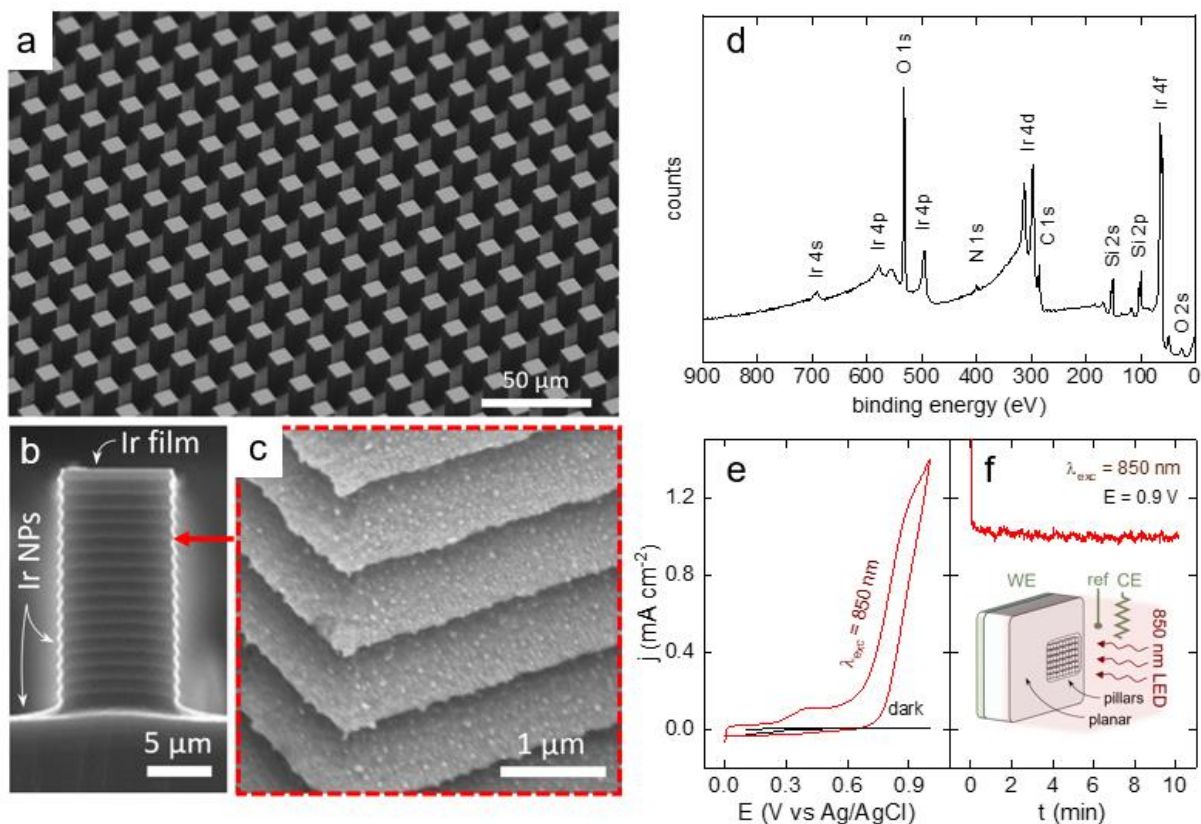


Figure 2. a-c) SEM (a) tilted image of $n\text{-Si}_{\text{MPs}}/\text{SiO}_x/\text{Ir}$, (b) cross-sectional view of a single $n\text{-Si}_{\text{MPs}}/\text{SiO}_x/\text{Ir}$ pillar, and (c) tilted view of a pillar sidewall (the red arrow on panel points approximately the corresponding area in (b)). d) XPS survey spectrum of $n\text{-Si}_{\text{MPs}}/\text{SiO}_x/\text{Ir}$. e) CVs measured with a “dual” $n\text{-Si}_{\text{plan}}\text{-}n\text{-Si}_{\text{MPs}}/\text{SiO}_x/\text{Ir}$ photoanode, in the dark (black curve) and under full-surface illumination (red curve, $\lambda_{\text{exc}} = 850 \text{ nm}$). f) CA recorded at $E = 0.9 \text{ V}$ under full-surface illumination ($\lambda_{\text{exc}} = 850 \text{ nm}$) with electrolyte circulation (1 mL s^{-1}). The inset depicts the electrochemical cell comprising the “dual” $n\text{-Si}_{\text{plan}}\text{-}n\text{-Si}_{\text{MPs}}$ photoanode under full-surface illumination. The electrolyte was composed of $5 \text{ mM } [\text{Ru}(\text{bpy})_3]^{2+}$ and 100 mM TPrA in PBS solution ($\text{pH} = 7.4$).

While a homogeneous MIS junction (such as that present on the top of the pillars) is expected to induce better stability towards *in situ* electrochemical passivation of Si^{28,44} it remains technologically difficult to conformally coat high-aspect-ratio micro and nanostructures with metal thin films.⁴⁵ In our case, the presence of dispersed metal NPs on the Si is not a problem since it is now well-known that inhomogeneous nanoscale MIS junctions can efficiently promote hole/liquid

charge transfer.^{37,46–50} Based on that, we expect that photogenerated charge transfer (thus, PECL) can occur over the whole Si surface area.

3.2 Electrochemical characterization

“Dual” $n\text{-Si}_{\text{plan}}\text{-Si}_{\text{MPs}}/\text{SiO}_x/\text{Ir}$ photoanodes, comprising, on the same surface, a planar $n\text{-Si}_{\text{plan}}$ and a microstructured $n\text{-Si}_{\text{MPs}}$ region were prepared. This photoanode design, depicted in the inset of **Figure 2f** (SEM are shown in Figure S1), was chosen because it allowed to perform the optical characterization in the same experimental conditions in both configurations (in the next experiments). **Figure 2e** presents typical cyclic voltammograms (CVs), recorded at a “dual” photoanode immersed in an electrolyte comprising $[\text{Ru}(\text{bpy})_3]^{2+}$ (5 mM) and TPrA (100 mM). In the dark (black curve), negligible current was produced, showing the inactivity of the system. Conversely, the illumination of the entire $n\text{-Si}_{\text{plan}}\text{-Si}_{\text{MPs}}/\text{SiO}_x/\text{Ir}$ photoanode with a near-IR light emitting diode (LED) ($\lambda_{\text{exc}} = 850 \text{ nm}$, $P_{\text{LED}} = 5 \text{ mW cm}^{-2}$) produced a photocurrent, which increased considerably at $E > 0.6 \text{ V}$ (all potentials in this article are reported vs. Ag/AgCl (3 M KCl)). This is perfectly in line with our previous report on planar $n\text{-Si}/\text{SiO}_x/\text{Ir}$ MIS photoanodes.²⁸ According to our previous study, this oxidation wave corresponds to the concomitant oxidation of TPrA and $[\text{Ru}(\text{bpy})_3]^{2+}$, accompanied by visible light generation at $\lambda_{\text{ECL}} = 632 \text{ nm}$, as depicted in **Figure 1a**.²⁸ A small oxidation wave at $\sim 0.4 \text{ V}$, not reported before,²⁸ was observed during the first CV scan (shown in the red curve of **Figure 2e**) and disappeared in subsequent scans (**Figure S3**). This wave is not identified and we attribute it to the oxidation of species present on the electrode surface (resulting from the manufacturing process). Then, a potentiostatic measurement ($E = 0.9 \text{ V}$) was performed under illumination of the entire $n\text{-Si}_{\text{plan}}\text{-Si}_{\text{MPs}}/\text{SiO}_x/\text{Ir}$ photoanode. In this case, a circulating electrolyte was employed to ensure a high mass transfer of the ECL reactants at the $n\text{-Si}_{\text{plan}}\text{-Si}_{\text{MPs}}/\text{SiO}_x/\text{Ir}$ surface and a more intense ECL signal. As shown in the

chronoamperometry (CA) of **Figure 1f**, a stable photocurrent ($j = 1 \text{ mA cm}^{-2}$) was recorded during 10 min, suggesting a good stability of the $n\text{-Si}_{\text{plan}}\text{-Si}_{\text{MPS}}/\text{SiO}_x/\text{Ir}$ photoanode, as required for the next localized PECL experiments that will be discussed in the following section.

3.3 Light-addressable PECL

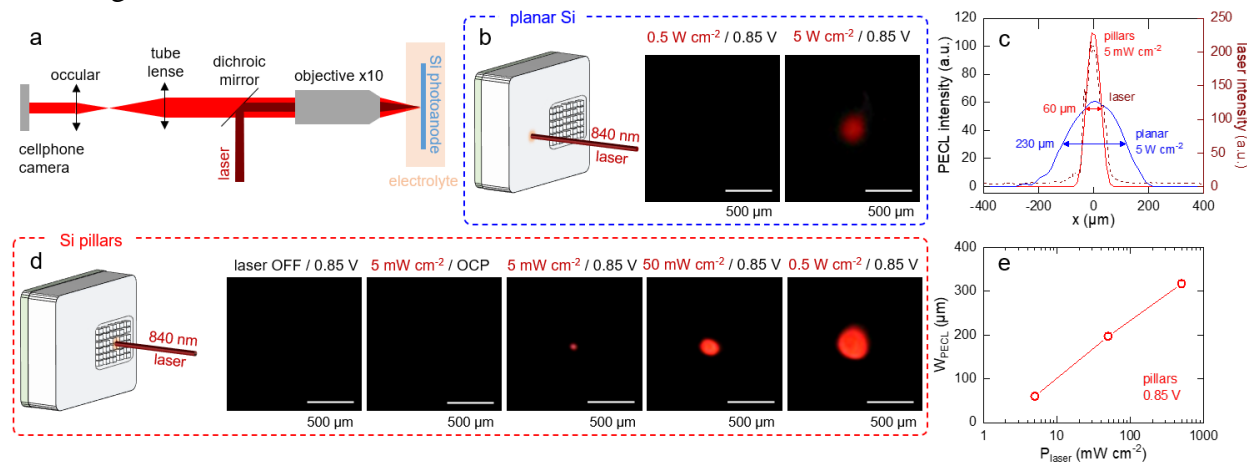


Figure 3. a) Optical setup used for light-addressable PECL measurements. b) Sketch of the experiment (left) and pictures of the PECL spots recorded on $n\text{-Si}_{\text{plan}}/\text{SiO}_x/\text{Ir}$ with $P_{\text{laser}} = 0.5$ and 5 W cm^{-2} , $E = 0.85 \text{ V}$. c) Intensity profiles of: the laser beam (brown dashed curve), the PECL spot recorded on $n\text{-Si}_{\text{plan}}/\text{SiO}_x/\text{Ir}$ at $P_{\text{laser}} = 5 \text{ W cm}^{-2}$ (blue curve) and the PECL spot recorded on $n\text{-Si}_{\text{MPS}}/\text{SiO}_x/\text{Ir}$ at $P_{\text{laser}} = 5 \text{ mW cm}^{-2}$ (red curve). d) Sketch of the experiment (left) and pictures of the PECL spots recorded on $n\text{-Si}_{\text{MPS}}/\text{SiO}_x/\text{Ir}$ with different P_{laser} values (0 to 5 W cm^{-2}) and different E (OCP or 0.85 V). e) Variations of the full-width at half-maximum W_{PECL} as a function of the laser power P_{laser} on $n\text{-Si}_{\text{MPS}}/\text{SiO}_x/\text{Ir}$. The electrolyte was composed of $5 \text{ mM } [\text{Ru}(\text{bpy})_3]^{2+}$, 100 mM TPrA in PBS ($\text{pH} = 7.4$). The electrolyte flow was 1 mL s^{-1} . $t_{\text{expo}} = 1/23 \text{ s}$.

Spatially-resolved PECL measurements were performed with a near-IR laser beam ($\lambda_{\text{exc}} = 840 \text{ nm}$) as the excitation source. The optical setup, shown in **Figure 3a**, enabled to focus the beam onto a selected area (Si_{plan} or Si_{MPS}) of the “dual” $n\text{-Si}_{\text{plan}}\text{-Si}_{\text{MPS}}/\text{SiO}_x/\text{Ir}$ electrode while recording the visible emission pattern through a table-top microscope apparatus (details are provided in Section 1.6, SI). The incident laser beam has a spot width (W_{laser}) of $60 \mu\text{m}$, as determined by its full width at half maximum (FWHM) (**Figure S4**), the beam profile of which is shown by the

dashed brown spectrum of **Figure 3c**. The laser beam ($\lambda_{\text{exc}} = 840 \text{ nm}$) was first projected on the $n\text{-Si}_{\text{plan}}/\text{SiO}_x/\text{Ir}$ region (**Figure 3b**) and, then, on the $n\text{-Si}_{\text{MPs}}/\text{SiO}_x/\text{Ir}$ region (**Figure 3d**). During these measurements, a constant potential of $E = 0.85 \text{ V}$ was imposed to the “dual” electrode and the exposure time of the camera (t_{expo}) was set to $1/23 \text{ s}$. Four orders of magnitude in laser power (P_{laser}) were employed, from $5 \cdot 10^{-3}$ to 5 W cm^{-2} . As seen in **Figure 3b**, no PECL spot was captured on the planar Si region when $P_{\text{laser}} \leq 0.5 \text{ W cm}^{-2}$. At 5 W cm^{-2} , a PECL spot with $W_{\text{PECL}} = 230 \mu\text{m}$ was captured. This value is 3.8 times higher than W_{laser} , as shown in the blue curve of **Figure 3c**. After that, the laser beam was spotted on the structured $n\text{-Si}_{\text{MPs}}/\text{SiO}_x/\text{Ir}$ region (**Figure 3d**). In this case, intense PECL could be recorded for a P_{laser} value as low as 5 mW cm^{-2} , i.e, below two orders of magnitude lower than the planar case. The larger efficiency of the $n\text{-Si}_{\text{MPs}}/\text{SiO}_x/\text{Ir}$ region compared to the planar one cannot be explained by the surface enhancement factor due to pillar structuration or changes of the optical properties of the electrode. However, the Bosch-process scalloping of the pillar sidewalls as well as the inhomogeneity of the Ir coating on these sidewalls could play a role in this phenomenon. The profile of the PECL spot at $P_{\text{laser}} = 5 \text{ mW cm}^{-2}$ is shown in **Figure 3c** (red curve). In this case, $W_{\text{PECL}} = 60 \mu\text{m}$, which was very similar to the previously determined W_{laser} (brown dashed curve). This demonstrates that a good spatial resolution can be obtained using our microstructuring strategy. **Figure 3d** also shows that the PECL spot width depends on P_{laser} , as plotted in **Figure 3e**. This trend can only be explained if one considers a saturation of the hole transfer rate from the semiconductor electrode to the electrolyte. Two control experiments, performed without illumination and without applying a potential (**Figure 3d**) confirm the necessity of simultaneous light excitation and potential application for triggering PECL. To sum up, these results show that the use of the $n\text{-Si}_{\text{MPs}}/\text{SiO}_x/\text{Ir}$ microstructures spatially confines

the light-addressable electrochemistry and drastically improves the brilliance, light sensitivity and spatial resolution of the local PECL signal.

3.4 Simulations

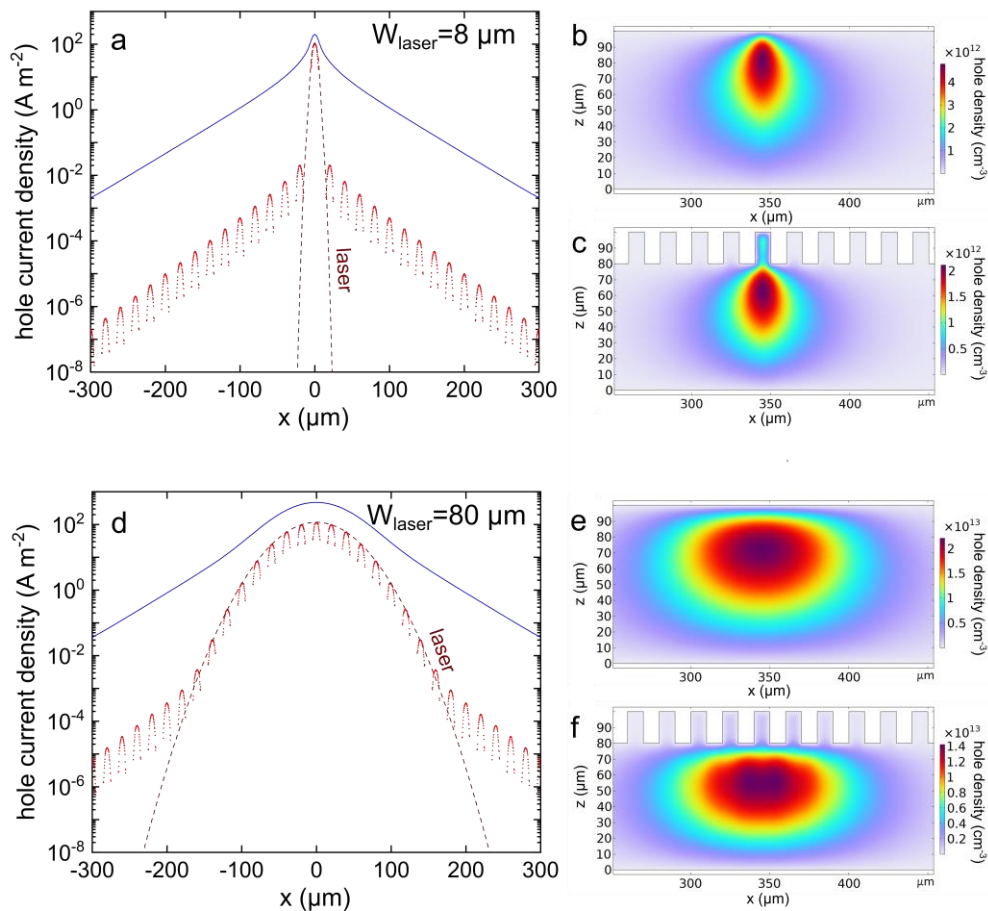


Figure 4. Results of the simulations performed with a-c) $W_{\text{laser}} = 8 \mu\text{m}$ and d-f) $W_{\text{laser}} = 80 \mu\text{m}$. a,d) Semilogarithmic plots of the hole current density as a function of the lateral position (x) on $n\text{-Si}_{\text{plan}}$ (blue curves) and $n\text{-Si}_{\text{MPs}}$ surfaces (red curves). b,c,e,f) Two-dimensional cross-section representations of the hole density as a function of depth (z) for (b,e) $n\text{-Si}_{\text{plan}}$ and (c,f) $n\text{-Si}_{\text{MPs}}$.

These results were rationalized by numerical simulations of carrier transport in the electrode using the COMSOL software (details are provided in Section 2, SI; input parameters are shown in **Table S1**). **Figure 4** shows the spatial profile of the hole current density at the semiconductor-electrolyte

interface (**Figures 4a,d**) and the steady-state hole density (**Figures 4b,c,e,f**) across the electrodes, for $n\text{-Si}_{\text{plan}}$ (blue curves in **Figures 4a,d** and cross-sections of **Figures 4b,e**) and $n\text{-Si}_{\text{MPs}}$ (red curves in **Figures 4a,d** and cross-sections of **Figures 4c,f**). Two W_{laser} values were used in the simulations: $8\ \mu\text{m}$ (i.e., lower than the width of a single pillar, **Figures 4a-c**) and $80\ \mu\text{m}$ (i.e., close to W_{laser} used in the previous experiments, **Figures 4d-f**). **Figures 4a,d** show that, for both types of surfaces, the hole current density can be described by two components. The first component features a spatial distribution close to the excitation profile (either 8 or $80\ \mu\text{m}$). It originates from the direct drift of carriers photogenerated within the SCL. The second component appears as lateral sidebands in the current density spatial profile with an exponential decay extending over several hundreds of μm away from the photoexcitation. This second component is the signature of hole diffusion deeper in the electrode. In $n\text{-Si}_{\text{plan}}$, the direct drift photocurrent contribution is only one order of magnitude larger than the diffusion contribution. In contrast, for $n\text{-Si}_{\text{MPs}}$, the diffusion sidebands are lowered by 4 to 5 orders of magnitude below the direct drift contribution. **Figures 4b,c,e,f** show the steady state hole density across the electrodes in the different configurations. They confirm the strong lateral diffusion of the deep photocarriers. Conversely, the fast drift of the holes generated within the SCL towards the interface and their subsequent injection into the electrolyte results in the decrease of the steady-state hole population in this region that does not reproduce the hole photogeneration profile. This drift/transfer mechanism is faster than the Shockley–Read–Hall recombination rate and it prevents diffusion from occurring for this part of the photogenerated carriers and their contribution to the current density reflects the illumination lateral profile. In the case of $n\text{-Si}_{\text{MPs}}$, microstructuring prevents lateral diffusion for a much larger fraction of the photocarriers controlled by the etching depth of the pillar structure ($20\ \mu\text{m}$) compared to planar electrodes for which the charge distribution is ruled by L_D and W_{SCL} .

3.5 Near-IR PECL imaging

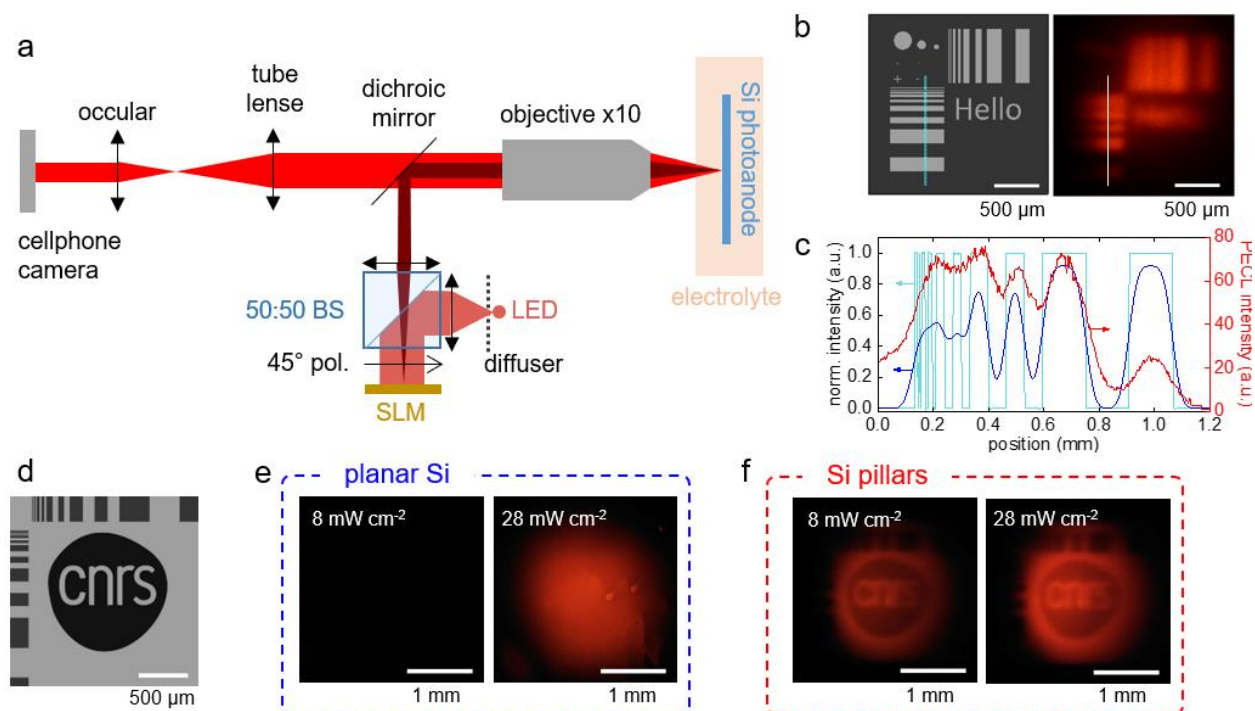


Figure 5. a) Optical setup employed for PECL near-IR imaging (pol. indicates a polarizer, BS indicates a beam splitter). b) Near-IR pattern projected by the SLM on the photoanode (left) and its corresponding PECL image on $n\text{-Si}_{\text{MPS}}/\text{SiO}_x/\text{Ir}$ with $P_{\text{LED}} = 28 \text{ mW cm}^{-2}$ and $t_{\text{expo}} = 1/3 \text{ s}$ (right). c) Intensity profile corresponding to the light blue line in left panel (b) (light blue curve), convolution of Gaussian curves having an FWHM of $60 \mu\text{m}$ with the light blue curve (dark blue curve), intensity profile of the PECL image, corresponding to the white line in panel (b) (red curve). d) Near-IR pattern projected by the SLM on the photoanode. e, f) Corresponding PECL images recorded on (e) $n\text{-Si}_{\text{plan}}/\text{SiO}_x/\text{Ir}$ and (f) $n\text{-Si}_{\text{MPS}}/\text{SiO}_x/\text{Ir}$ for $P_{\text{LED}} = 8$ and 28 mW cm^{-2} , with $t_{\text{expo}} = 1 \text{ s}$. The electrolyte was composed of $5 \text{ mM } [\text{Ru}(\text{bpy})_3]^{2+}$, 100 mM TPrA in PBS solution ($\text{pH} = 7.4$). The electrolyte flow was 1 mL s^{-1} . $E = 0.85 \text{ V}$.

Next, as shown in **Figure 5a**, a near-IR ($\lambda_{\text{exc}} = 850 \text{ nm}$) pattern was projected from the phase-only LCOS-SLM on the electrode surface. First, a near-IR pattern comprising a series of microbands and the word “Hello”, shown in **Figure 5b**, were projected onto a biased ($E = 0.85 \text{ V}$) $n\text{-Si}_{\text{MPS}}/\text{SiO}_x/\text{Ir}$ photoanode surface. The corresponding PECL pattern is shown on the right of **Figure 5b**. The intensity profile of the band patterns extracted along the light-blue line on the left of

Figure 5b is depicted by the light blue curve in **Figure 5c**. The corresponding PECL signal is also plotted in red in **Figure 5c**. Note that the decrease of PECL intensity over the line profile from the top (0 mm) to the bottom (1.2 mm) is a consequence of the inhomogeneity of near-IR illumination of the SLM. From the horizontal bands of the projected image (**Figure 5b**, right) and the intensity profiles (**Figure 5c** red curve), the four widest bands are well-defined but the narrowest bands are not resolved. A convolution of the illumination profile (light blue curve in **Figure 5c**) using a Gaussian profile with a 60 μm -wide FWHM is plotted in dark blue in **Figure 5c**. It shows a relatively good agreement with the experimental signal (**Figure 5c**, red curve) except for the overall illumination inhomogeneity mentioned above. This consistency confirms the 60 μm spatial resolution of PECL imaging with $n\text{-Si}_{\text{MPs}}$ suggested by the first experiments. It is three times larger than the pitch of the pillar array. This limited resolution explains why the word “Hello” is blurred and hardly readable in **Figure 5b**. The difference between this experimental resolution and the one inferred to the control of carrier diffusion by microstructuring in simulation (limited to the size of a single pillar) suggests that another phenomenon is at play. A local saturation of the carrier transfer rate to the electrolyte is possible.

Finally, a slightly larger near-IR pattern, suiting to the 60 μm spatial resolution of the present system, composed by the CNRS logo (**Figure 5d**, the width of the letters is 55 μm), was projected on $n\text{-Si}_{\text{plan}}/\text{SiO}_x/\text{Ir}$ (**Figure 5e**) and $n\text{-Si}_{\text{MPs}}/\text{SiO}_x/\text{Ir}$ (**Figure 5f**) with $P_{\text{LED}} = 8$ or 28 mW cm^{-2} . The image pattern was recorded with $t_{\text{expo}} = 1$ s. On the planar $n\text{-Si}_{\text{plan}}/\text{SiO}_x/\text{Ir}$ photoanode, **Figure 5e** shows no measured PECL at $P_{\text{LED}} = 8$ mW cm^{-2} and that no pattern could be observed at $P_{\text{LED}} = 28$ mW cm^{-2} , because of the excessive lateral diffusion of holes. Contrarywise, on the structured $n\text{-Si}_{\text{MPs}}/\text{SiO}_x/\text{Ir}$ photoanode, **Figure 5f** displays an easily readable CNRS logo in the PECL image, with a relatively dark circle background at $P_{\text{LED}} = 8$ and 28 mW cm^{-2} . These near-IR imaging

experiments further confirmed that the $n\text{-Si}_{\text{MPs}}/\text{SiO}_x/\text{Ir}$ structure decreases lateral hole diffusion and demonstrated a significantly improved resolution for near-IR imaging. A video (accessible in SI) acquired with an animated logo demonstrates that this PECL-based near-IR-to-visible image converter operates in real-time without lag.

4. CONCLUSION

In this work, we have studied the localized IR ($\lambda_{\text{exc}} = 840$ or 850 nm)-to-visible ($\lambda_{\text{ECL}} = 632$ nm) PECL conversion at planar and microstructured MIS $n\text{-Si}/\text{SiO}_x/\text{Ir}$ photoanodes using the model $[\text{Ru}(\text{bpy})_3]^{2+}$ -TPrA ECL system. By comparing the PECL images obtained with planar $n\text{-Si}_{\text{plan}}/\text{SiO}_x/\text{Ir}$ and microstructured $n\text{-Si}_{\text{MPs}}/\text{SiO}_x/\text{Ir}$ photoanodes and confronting these results with numerical transport simulations within the electrodes, the use of micropillar array is shown to confine photogenerated holes, leading to a considerably improved image-conversion spatial resolution. As such, these results present the first example of near-IR PECL imaging. In addition, our approach provides a general solution for light-addressable electrochemistry on Si, which is complementary to the use of an $a\text{-Si}$ overlayer,⁸⁻¹¹ (note that $a\text{-Si}$ has been reported inefficient in the specific case of PECL).²⁵ In these proof-of-principle experiments, we measured a resolution of $60\ \mu\text{m}$, a factor of three above the value expected from transport simulations indicating room for improvements, most likely in the optimization of the carrier transfer rates to the electrolyte. Improving further the imaging resolution could be possible through the management of the photocarrier diffusion length by either reducing the pillar dimensions, using direct band gap materials, or non-stoichiometric and heavy metal doped materials. These results open doors to the development of original light conversion devices implying a liquid phase, that may involve cheaper manufacturing or improved flexibility compared to all-solid devices. This concept has the potential to lead to original applications in photothermal imaging and analysis.

SUPPORTING INFORMATION

We provide supporting information on numerical simulations, SEM characterization, CV characterization and imaging. A real-time movie showing the time response of the imaging device is also provided. Raw data are available on request.

AUTHORS' CONTRIBUTIONS

The manuscript was written through the contributions of all authors. All authors have approved the final version of the manuscript.

Funding Sources

ANR (LiCORN, ANR-20-CE29-0006)

ACKNOWLEDGMENT

This work was funded by ANR (LiCORN, ANR-20-CE29-0006). Loic Joanny and Francis Gouttefangeas (ScanMat/CMEBA) are acknowledged for SEM. The XPS platform and Dr. Corinne Lagrost (Univ Rennes, CNRS, ScanMat), UAR2025, are acknowledged for XPS analysis. The NanoRennes platform and Renatech+ network are acknowledged for additional clean room processing.

REFERENCES

- (1) Vogel, Y. B.; Gooding, J. J.; Ciampi, S. Light-Addressable Electrochemistry at Semiconductor Electrodes: Redox Imaging, Mask-Free Lithography and Spatially Resolved Chemical and Biological Sensing. *Chem. Soc. Rev.* **2019**, *48*, 3723–3739.
- (2) Meng, Y.; Chen, F.; Wu, C.; Krause, S.; Wang, J.; Zhang, D.-W. Light-Addressable Electrochemical Sensors toward Spatially Resolved Biosensing and Imaging Applications.

- ACS Sensors* **2022**, *7*, 1791–1807.
- (3) Terrero Rodríguez, I. M.; Borrill, A. J.; Schaffer, K. J.; Hernandez, J. B.; O’Neil, G. D. Light-Addressable Electrochemical Sensing with Electrodeposited n-Silicon/Gold Nanoparticle Schottky Junctions. *Anal. Chem.* **2020**, *92*, 11444–11452.
 - (4) Hernandez, J. B.; Epright, Z. D.; Terrero Rodríguez, I. M.; O’Neil, G. D. Electrodeposition Parameters Dramatically Influence the Morphology, Stability, and Performance of n-Si/Pt Light-Addressable Electrochemical Sensors. *ChemElectroChem* **2023**, *10*, e202300400.
 - (5) Seo, D.; Lim, S. Y.; Lee, J.; Yun, J.; Chung, T. D. Robust and High Spatial Resolution Light Addressable Electrochemistry Using Hematite (α -Fe₂O₃) Photoanodes. *ACS Appl. Mater. Interfaces* **2018**, *10*, 33662–33668.
 - (6) Wu, F.; Campos, I.; Zhang, D.-W.; Krause, S. Biological Imaging Using Light-Addressable Potentiometric Sensors and Scanning Photo-Induced Impedance Microscopy. *Proc. R. Soc. A Math. Phys. Eng. Sci.* **2017**, *473*, 20170130.
 - (7) Inoue, T.; Fujishima, A.; Honda, K. Photoelectrochemical Imaging Processes Using Semiconductor Electrodes. *Chem. Lett.* **1978**, *7*, 1197–1200.
 - (8) Suzurikawa, J.; Nakao, M.; Kanzaki, R.; Takahashi, H. Microscale PH Gradient Generation by Electrolysis on a Light-Addressable Planar Electrode. *Sensors Actuators B Chem.* **2010**, *149*, 205–211.
 - (9) Lim, S. Y.; Kim, Y.-R.; Ha, K.; Lee, J.-K.; Lee, J. G.; Jang, W.; Lee, J.-Y.; Bae, J. H.; Chung, T. D. Light-Guided Electrodeposition of Non-Noble Catalyst Patterns for Photoelectrochemical Hydrogen Evolution. *Energy Environ. Sci.* **2015**, *8*, 3654–3662.
 - (10) Vogel, Y. B.; Gonçalves, V. R.; Al-Obaidi, L.; Gooding, J. J.; Darwish, N.; Ciampi, S. Nanocrystal Inks: Photoelectrochemical Printing of Cu₂O Nanocrystals on Silicon with 2D Control on Polyhedral Shapes. *Adv. Funct. Mater.* **2018**, *28*, 1804791.
 - (11) Lian, J.; Tang, W.; Yang, Y.; Vaidyanathan, R.; Gonçalves, V. R.; Arman, S. Y.; Tilley, R. D.; Gooding, J. J. A Transparent Semiconducting Surface for Capturing and Releasing

- Single Cells from a Complex Cell Mixture. *ACS Appl. Mater. Interfaces* **2022**, *14*, 18079–18086.
- (12) Liu, Z.; Qi, W.; Xu, G. Recent Advances in Electrochemiluminescence. *Chem. Soc. Rev.* **2015**, *44*, 3117–3142.
- (13) Sojic, N. *Analytical Electrogenenerated Chemiluminescence: From Fundamentals to Bioassays*; RSC, Ed.; Detection Science; The Royal Society of Chemistry, 2020.
- (14) Gou, X.; Xing, Z.; Ma, C.; Zhu, J.-J. A Close Look at Mechanism, Application, and Opportunities of Electrochemiluminescence Microscopy. *Chem. Biomed. Imaging* **2023**, *1*, 414–433.
- (15) Guo, M.; Du, D.; Wang, J.; Ma, Y.; Yang, D.; Haghghatbin, M. A.; Shu, J.; Nie, W.; Zhang, R.; Bian, Z.; Wang, L.; Smith, Z. J.; Cui, H. Three-Biomarker Joint Strategy for Early and Accurate Diagnosis of Acute Myocardial Infarction via a Multiplex Electrochemiluminescence Immunoarray Coupled with Robust Machine Learning. *Chem. Biomed. Imaging* **2023**, *1*, 179–185.
- (16) Li, L.; Chen, Y.; Zhu, J.-J. Recent Advances in Electrochemiluminescence Analysis. *Anal. Chem.* **2017**, *89*, 358–371.
- (17) Zanut, A.; Fiorani, A.; Canola, S.; Saito, T.; Ziebart, N.; Rapino, S.; Rebecani, S.; Barbon, A.; Irie, T.; Josel, H.-P.; Negri, F.; Marcaccio, M.; Windfuhr, M.; Imai, K.; Valenti, G.; Paolucci, F. Insights into the Mechanism of Coreactant Electrochemiluminescence Facilitating Enhanced Bioanalytical Performance. *Nat. Commun.* **2020**, *11*, 2668.
- (18) Zhao, Y.; Bouffier, L.; Xu, G.; Loget, G.; Sojic, N. Electrochemiluminescence with Semiconductor (Nano)Materials. *Chem. Sci.* **2022**, *13*, 2528–2550.
- (19) Laser, D.; Bard, A. J. Semiconductor Electrodes. Photo-Induced Electrogenenerated Chemiluminescence and up-Conversion at Semiconductor Electrodes. *Chem. Phys. Lett.* **1975**, *34*, 605–610.
- (20) Luttmer, J. D.; Bard, A. J. Electrogenenerated Chemiluminescence: 34. Photo-Induced

- Electrogenerated Chemiluminescence and Up-Conversion at Semiconductor Electrodes. *J. Electrochem. Soc.* **1979**, *126*, 414–419.
- (21) Xue, J.-W.; Xu, C.-H.; Zhao, W.; Chen, H.-Y.; Xu, J.-J. Photoinduced Electrogenerated Chemiluminescence Imaging of Plasmonic Photoelectrochemistry at Single Nanocatalysts. *Nano Lett.* **2023**, *23*, 4572–4578.
- (22) Zhao, Y.; Yu, J.; Xu, G.; Sojic, N.; Loget, G. Photoinduced Electrochemiluminescence at Silicon Electrodes in Water. *J. Am. Chem. Soc.* **2019**, *141*, 13013–13016.
- (23) Yu, J.; Saada, H.; Abdallah, R.; Loget, G.; Sojic, N. Luminescence Amplification at BiVO₄ Photoanodes by Photoinduced Electrochemiluminescence. *Angew. Chem. Int. Ed.* **2020**, *59*, 15157–15160.
- (24) Zhao, Y.; Descamps, J.; Hoda Al Bast, N.; Duque, M.; Esteve, J.; Sepulveda, B.; Loget, G.; Sojic, N. All-Optical Electrochemiluminescence. *J. Am. Chem. Soc.* **2023**, *145*, 17420–17426.
- (25) Vogel, Y. B.; Darwish, N.; Ciampi, S. Spatiotemporal Control of Electrochemiluminescence Guided by a Visible Light Stimulus. *Cell Rep. Phys. Sci.* **2020**, *1*, 100107.
- (26) Descamps, J.; Zhao, Y.; Goudeau, B.; Manojlovic, D.; Loget, G.; Sojic, N. Infrared Photoinduced Electrochemiluminescence Microscopy of Single Cells. *Chem. Sci.* **2023**.
- (27) Nicholson, M. M. Photoelectrochemical Image Conversion. *J. Electrochem. Soc.* **1972**, *119*, 461.
- (28) Zhao, Y.; Descamps, J.; Ababou-Girard, S.; Bergamin, J.-F.; Santinacci, L.; Léger, Y.; Sojic, N.; Loget, G. Metal-Insulator-Semiconductor Anodes for Ultrastable and Site-Selective Upconversion Photoinduced Electrochemiluminescence. *Angew. Chem. Int. Ed.* **2022**, *61*, e2022018.
- (29) Boyd, I. W.; Binnie, T. D.; Wilson, J. I. B.; Colles, M. J. Absorption of Infrared Radiation in Silicon. *J. Appl. Phys.* **1984**, *55*, 3061–3063.

- (30) Franssila, S.; Sainiemi, L. Reactive Ion Etching (RIE) BT - Encyclopedia of Microfluidics and Nanofluidics; Li, D., Ed.; Springer US: Boston, MA, 2008; pp 1772–1781.
- (31) Bae, D.; Seger, B.; Vesborg, P. C. K.; Hansen, O.; Chorkendorff, I. Strategies for Stable Water Splitting via Protected Photoelectrodes. *Chem. Soc. Rev.* **2017**, *46*, 1933–1954.
- (32) Sun, K.; Shen, S.; Liang, Y.; Burrows, P. E.; Mao, S. S.; Wang, D. Enabling Silicon for Solar-Fuel Production. *Chem. Rev.* **2014**, *114*, 8662–8719.
- (33) Shaner, M. R.; Hu, S.; Sun, K.; Lewis, N. S. Stabilization of Si Microwire Arrays for Solar-Driven H₂O Oxidation to O₂(g) in 1.0 M KOH(Aq) Using Conformal Coatings of Amorphous TiO₂. *Energy Environ. Sci.* **2015**, *8*, 203–207.
- (34) Ciampi, S.; Guan, B.; Darwish, N.; Reece, P. J.; Gooding J. J. Redox-Active Monolayers in Mesoporous Silicon. *J. Phys. Chem. C* **2012**, *116*, 16080-16088.
- (35) Loget, G.; Mériadec, C.; Dorcet, V.; Fabre, B.; Vacher, A.; Fryars, S.; Ababou-Girard, S. Tailoring the Photoelectrochemistry of Catalytic Metal-Insulator-Semiconductor (MIS) Photoanodes by a Dissolution Method. *Nat. Commun.* **2019**, *10*, 3522.
- (36) Digdaya, I. A.; Adhyaksa, G. W. P.; Trzeźniewski, B. J.; Garnett, E. C.; Smith, W. A. Interfacial Engineering of Metal-Insulator-Semiconductor Junctions for Efficient and Stable Photoelectrochemical Water Oxidation. *Nat. Commun.* **2017**, *8*, 15968.
- (37) Loget, G.; Fabre, B.; Fryars, S.; Mériadec, C.; Ababou-Girard, S. Dispersed Ni Nanoparticles Stabilize Silicon Photoanodes for Efficient and Inexpensive Sunlight-Assisted Water Oxidation. *ACS Energy Lett.* **2017**, *2*, 569–573.
- (38) Hemmerling, J. R.; Mathur, A.; Linic, S. Design Principles for Efficient and Stable Water Splitting Photoelectrocatalysts. *Acc. Chem. Res.* **2021**, *54*, 1992–2002.
- (39) Oh, K.; Joanny, L.; Gouttefangeas, F.; Fabre, B.; Dorcet, V.; Lassalle-Kaiser, B.; Vacher, A.; Mériadec, C.; Ababou-Girard, S.; Loget, G. Black Silicon Photoanodes Entirely Prepared with Abundant Materials by Low-Cost Wet Methods. *ACS Appl. Energy Mater.* **2019**, *2*, 1006–1010.

- (40) Chen, Y. W.; Prange, J. D.; Dühnen, S.; Park, Y.; Gunji, M.; Chidsey, C. E. D.; McIntyre, P. C. Atomic Layer-Deposited Tunnel Oxide Stabilizes Silicon Photoanodes for Water Oxidation. *Nat Mater* **2011**, *10*, 539–544.
- (41) Zhao, Y.; Descamps, J.; Le Corre, B.; Léger, Y.; Kuhn, A.; Sojic, N.; Loget, G. Wireless Anti-Stokes Photoinduced Electrochemiluminescence at Closed Semiconducting Bipolar Electrodes. *J. Phys. Chem. Lett.* **2022**, *13*, 5538–5544.
- (42) Descamps, J.; Zhao, Y.; Le-Pouliquen, J.; Goudeau, B.; Garrigue, P.; Tavernier, K.; Léger, Y.; Loget, G.; Sojic, N. Local Reactivity of Metal–Insulator–Semiconductor Photoanodes Imaged by Photoinduced Electrochemiluminescence Microscopy. *Chem. Commun.* **2023**, *59*, 12262–12265.
- (43) Moulder, J. F.; Stickle, W.; Sobol, W.; Bomben, K. D. *Handbook of X-Ray Photoelectron Spectroscopy A Reference Book of Standard Spectra for Identification and Interpretation of XPS Data*; Chastain, J., Ed.; Perkin Elmer Corp.: Eden Prairie, 1992.
- (44) Kenney, M. J.; Gong, M.; Li, Y.; Wu, J. Z.; Feng, J.; Lanza, M.; Dai, H. High-Performance Silicon Photoanodes. *Science* **2013**, *342*, 836–841.
- (45) Schlicht, S.; Haschke, S.; Mikhailovskii, V.; Manshina, A.; Bachmann, J. Highly Reversible Water Oxidation at Ordered Nanoporous Iridium Electrodes Based on an Original Atomic Layer Deposition. *ChemElectroChem* **2018**, *5*, 1259–1264.
- (46) Hill, J. C.; Landers, A. T.; Switzer, J. A. An Electrodeposited Inhomogeneous Metal–Insulator–Semiconductor Junction for Efficient Photoelectrochemical Water Oxidation. *Nat. Mater.* **2015**, *14*, 1150–1155.
- (47) Lee, S. A.; Lee, T. H.; Kim, C.; Lee, M. G.; Choi, M.-J.; Park, H.; Choi, S.; Oh, J.; Jang, H. W. Tailored NiO_x/Ni Cocatalysts on Silicon for Highly Efficient Water Splitting Photoanodes via Pulsed Electrodeposition. *ACS Catal.* **2018**, *8*, 7261–7269.
- (48) Hemmerling, J. R.; Mathur, A.; Linic, S. Characterizing the Geometry and Quantifying the Impact of Nanoscopic Electrocatalyst/Semiconductor Interfaces under Solar Water Splitting Conditions. *Adv. Energy Mater.* **2022**, *12*, 2103798.

- (49) Laskowski, F. A. L.; Oener, S. Z.; Nellist, M. R.; Gordon, A. M.; Bain, D. C.; Fehrs, J. L.; Boettcher, S. W. Nanoscale Semiconductor/Catalyst Interfaces in Photoelectrochemistry. *Nat. Mater.* **2020**, *19*, 69–76.
- (50) Loget, G. Water Oxidation with Inhomogeneous Metal-Silicon Interfaces. *Curr. Opin. Colloid Interface Sci.* **2019**, *39*, 40–50.

TOC Figure:

